Huang, J., Gong, X., Zhang, Q., Scarpa, F., Liu, Y., & Leng, J. (2016). In-plane mechanics of a novel zero Poisson's ratio honeycomb core. *Composites Part B: Engineering*, *89*, 67-76. https://doi.org/10.1016/j.compositesb.2015.11.032

In-plane mechanics of a novel zero Poisson's ratio honeycomb core

Jian Huang[a,b,c], Xiaobo Gong[c], Qiuhua Zhang[a], Fabrizio Scarpa[b,*], Yanju Liu[a], Jinsong Leng[c,*]
[a] *Department of Aerospace Science and Mechanics, No. 92 West Dazhi Street, Harbin Institute of Technology (HIT), P.O. Box 301, Harbin 150080, PR China*
[b] *Advanced Composites Center for Innovation and Science, University of Bristol, Bristol BS8 1TR, UK*
[c] *Center for Composite Materials and Structures, No. 2 Yikuang Street, Science Park of Harbin Institute of Technology (HIT), P.O. Box 301, Harbin, PR China*

Abstract: This work presents a novel zero in-plane Poisson's ratio honeycomb design for large out-of-plane deformations and morphing. The novel honeycomb topology is composed by two parts that provide separate in-plane and out-of-plane deformations contributions. The hexagonal component generates the out-of-plane load-bearing compression and in-plane compliance, while a thin plate part that connects the hexagonal section delivers the out-of-plane flexibility. The paper illustrates the in-plane mechanical properties through a combination of theoretical analysis, FE homogenization and experimental tests. Parametric analyses are also carried out to determine the dependence of the in-plane stiffness versus the geometric parameters that define the zero-ν honeycomb.

Keywords: A Honeycomb; B Mechanical properties; C Analytical modelling; D Mechanical testing.

1. Introduction

Honeycomb structures have drawn worldwide attention within the research community for their remarkable lightweight and mechanical properties, which are directly dependent upon the shape, topology and size of their cells [1, 2]. Different honeycomb configurations lead to different in-plane Poisson's ratio values. The in-plane Poisson's ratio of a conventional regular hexagonal honeycomb is theoretically equal to 1 when pure bending of the honeycomb ribs is the main deformation taken into account [1]. In general, however, centersymmetric hexagonal configurations exhibit both large positive (PPR) or negative (NPR) Poisson's ratio values [3-7]. The hexachiral [8-11], tetrachiral [9-11], and anti-tetrachiral [12] ones show negative in-plane Poisson's ratios (NPR). Honeycombs with negative Poisson's ratio are also described as auxetic [13, 14]. Honeycomb configurations like the SILICOMB [15-18], chevron [19-21] and accordion [22, 23] can however achieve a Poisson's ratio (ν) of zero (ZPR). ZPR honeycombs show no lateral mechanical coupling under in-plane deformation when loaded along one direction [16, 18]. The out-of-plane deformation of PPR honeycombs exhibits anticlastic or saddle-shape curvature that does not facilitate their use in sandwich structures with complex out-of-plane geometry [24-27]. Structures with NPR behavior feature synclastic curvature when subjected to out-of-plane bending [9, 24, 26, 28]. On the opposite, no anticlastic or synclastic curvature could be found for structures exhibiting ZPR under

* Corresponding author
E-mail address: lengjs@hit.edu.cn (Jinsong Leng); f.scarpa@bristol.ac.uk (Fabrizio Scarpa).

out-of-plane bending, which makes zero-ν cellular configurations more suitable for cylindrical sandwich panels and morphing applications in which the structure needs either to undergo pure cylindrical bending or one-dimensional (span) morphing [18, 19]. The chevron and accordion honeycombs feature ZPR by balancing the deformation between embedded re-entrant and non-re-entrant structures [19, 20, 22, 23]. The SILICOMB features a zero-ν behaviour by using a geometry inspired to the tessellation of the β-cristobalite lattice [29, 30]. One example of application of ZPR honeycombs with accordion-like honeycomb microstructures is biomedical scaffolds [31], and in the field of morphing aircraft flexible sandwich structures with cellular cores and flexible face sheets have been proposed as a promising solution for morphing skins [23, 32, 33]. ZPR honeycombs have been used in flexible skins undergoing one-dimensional spanwise morphing [22, 23, 32, 33] and have also demonstrated their potential in planar morphing applications [34]. Generally, morphing wing designs could be classified into in-plane and out-of-plane morphing [35-38], and spanwise morphing is a subset of the in-plane category. Moreover, the effect of the zero Poisson's ratio creates very complex and sometimes unusual multiphysics properties, like in the case of the strong increase of the longitudinal wave speed in a stressed plate with constrained width when the material has a ZPR behavior [39].

In this work, a novel honeycomb design exhibiting ZPR for large out-of-plane deformations is proposed and investigated. This honeycomb configuration features a new mechanism to achieve ZPR, which consists in inserting a hexagonal part to bear the out-of-plane compression and to produce in-plane flexibility, and connecting a thin plate for the large out-of-plane flexibility. Thus different parts bring about different mechanical properties leading to a separately design for the in-plane and out-of-plane performances. Analytical models to describe the in-plane elastic constants of the novel honeycomb are developed and benchmarked with the FE homogenization approaches and experimental tests. The sensitivity of the in-plane stiffness versus the honeycomb geometry is further investigated using a combination of analytical analysis and FE homogenization.

2. Models and experimental tests

2.1. Geometry of the novel honeycomb

Fig. 1 shows the representative unit cells of the novel ZPR honeycomb configuration with cell angles $\theta \geqslant 0$ and $\theta < 0$. The parameters l and $h=\alpha l$ are the length of the inclined wall and the vertical wall, respectively. The thickness of the hexagonal section, thin plate and the whole honeycomb are represented by $t=\beta l$, $b_1=\lambda b$ and b. The dimension $l_1=\eta l$ represents the length of the thin plate part. The parameter $b=\gamma l$ is used to normalize all dimensions. The width of the unit cell for the case $\theta \geqslant 0$ is $w=\alpha l+2l\sin(\theta)$ and becomes $w=\alpha l$ when $\theta < 0$.

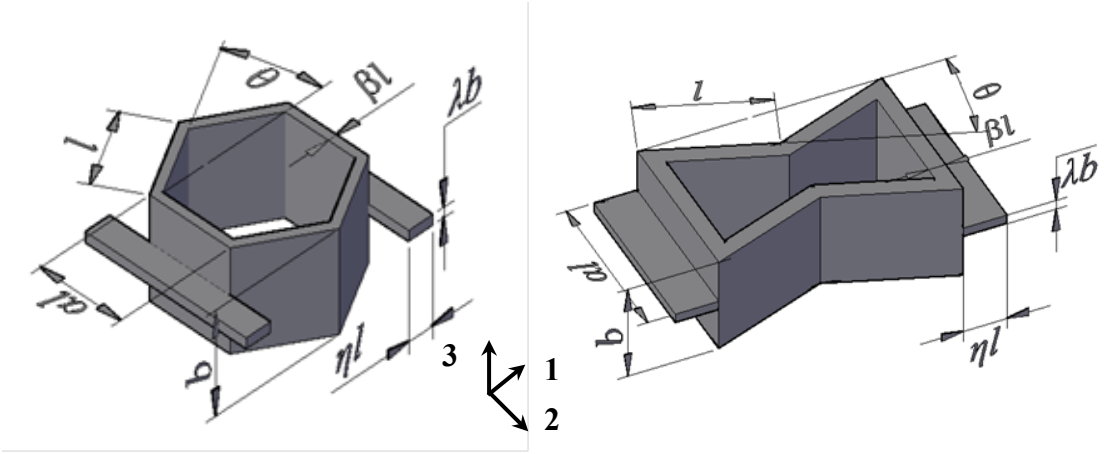

Fig.1. Geometry of the novel ZPR honeycomb unit cell with cell angle $\theta \geq 0$ and $\theta < 0$

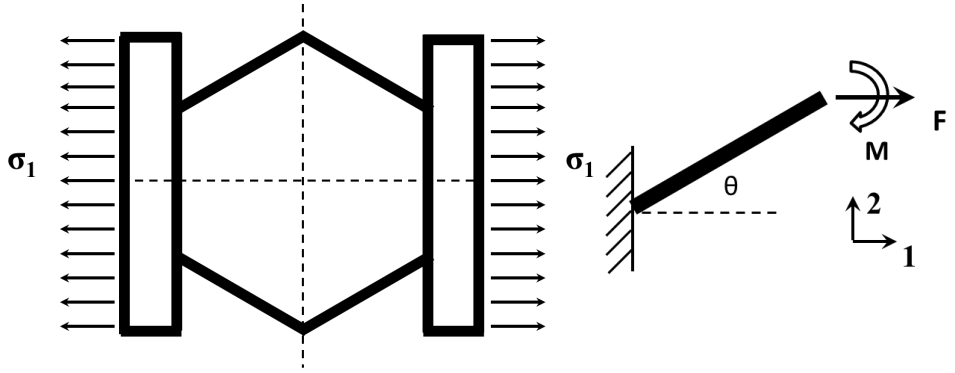

Fig.2. Top view of unit cell model to calculate the theoretical elastic modulus along the 1 (horizontal) direction for $\theta \geq 0$

2.2. Analytical models

Because the hexagonal structures of the honeycomb are connected by the thin plate and the hexagones structures are not directly in contact, one can infer that the in-plane Poisson's ratio v_{12} of the honeycomb is approximately equal to 0. The analytical models for the calculation of the in-plane elastic modulus along 1 (horizontal) direction developed in this work is based on the application of Castigliano's second theorem [40]. The honeycomb ribs are assumed to undergo bending and axial tensile deformations to avoid an infinite value of the homogenized Young's modulus when the internal cell angle equals to zero [1]. The theorem states that when an elastic system is staticallly loaded, the partial derivative of the strain energy U with respect to any applied force P_i equals the displacement δ_i of the point in which the force is applied:

$$\frac{\partial U}{\partial P_i} = \delta_i \tag{1}$$

For the case of a beam undergoing bending $M(x)$ and axial loading $F_N(x)$ one obtains:

$$U = \int_0^L \frac{M^2(x)}{2EI} dx + \int_0^L \frac{F_N{}^2(x)}{2EA} dx \tag{2}$$

The elastic modulus of the honeycomb is calculated following the loading scheme shown in Fig.2. One set of cell walls of length l are bent and stretched by the applied stress σ_1 parallel to 1 direction. From the equilibrium equations one can obtain the moment M bending the wall [1]:

$$M = \frac{l}{2} F l \sin\theta \tag{3}$$

It is worth noticing that the positive bending moment is orientated along the anti-clockwise direction . The bending moment distribution on the single rib is:

$$M(x) = (\frac{l}{2} l - x) F \sin\theta, F_N(x) = F \cos\theta \tag{4}$$

Substituting equation (4) into equation (2), one obtains the strain energy of the single bending wall:

$$U = \frac{F^2 l^3 \sin^2\theta}{24 E_s I} + \frac{F^2 l \cos^2\theta}{2 E_s A} \tag{5}$$

In (5), E_s is the Young's modulus of the honeycomb material, I and A the second moment of area and the area of the cross section respectively. Following equation (1) it is possible to obtain the horizontal displacement of the free end:

$$\delta_1 = \frac{F l^3 \sin^2\theta}{12 E_s I} + \frac{F l \cos^2\theta}{E_s A} \tag{6}$$

The homogenized stress and strain along the 1 (horizontal) direction for a cell angle $\theta \geq 0$ can be therefore obtained as:

$$\sigma_1 = \frac{F}{b(\frac{l}{2}\alpha l + l \sin\theta)}$$
$$\varepsilon_1 = \frac{\delta_1}{\eta l + l \cos\theta} \tag{7}$$

The homogenized and nondimensional Young's modulus along the 1 direction with a $\theta \geq 0$ cell angle can therefore be obtained from the ratio between the tensile stress and strain:

$$\frac{E_1}{E_s} = \frac{\beta^3(\eta + \cos\theta)}{(\frac{l}{2}\alpha + \sin\theta)(\sin^2\theta + \beta^2 \cos^2\theta)} \tag{8}$$

For the case of the honeycomb with a cell angle θ<0, following the same calculation procedures and when considering the width of the unit cell equal to αl (and equal to $\alpha l+2l\sin(\theta)$ when θ≥0), equation (7) can be rewritten as:

$$\varepsilon_1 = \frac{\delta_1}{\eta l + l\cos\theta}$$
$$\sigma_1 = \frac{2F}{b\alpha l} \tag{9}$$

Therefore, the homogenized and nondimensional elastic modulus along the 1 direction with the cell angle θ<0 (i.e., re-entrant configuration) can be calculated as:

$$\frac{E_1}{E_s} = \frac{2\beta^3(\eta+\cos\theta)}{\alpha(\sin^2\theta+\beta^2\cos^2\theta)} \tag{10}$$

In summary, the elastic modulus of the novel ZPR honeycomb along the 1 direction can be expressed as:

$$\frac{E_1}{E_s} = \begin{cases} \dfrac{\beta^3(\eta+\cos\theta)}{(\frac{1}{2}\alpha+\sin\theta)(\sin^2\theta+\beta^2\cos^2\theta)} & for\ \theta \geq 0 \\ \dfrac{2\beta^3(\eta+\cos\theta)}{\alpha(\sin^2\theta+\beta^2\cos^2\theta)} & for\ \theta < 0 \end{cases} \tag{11}$$

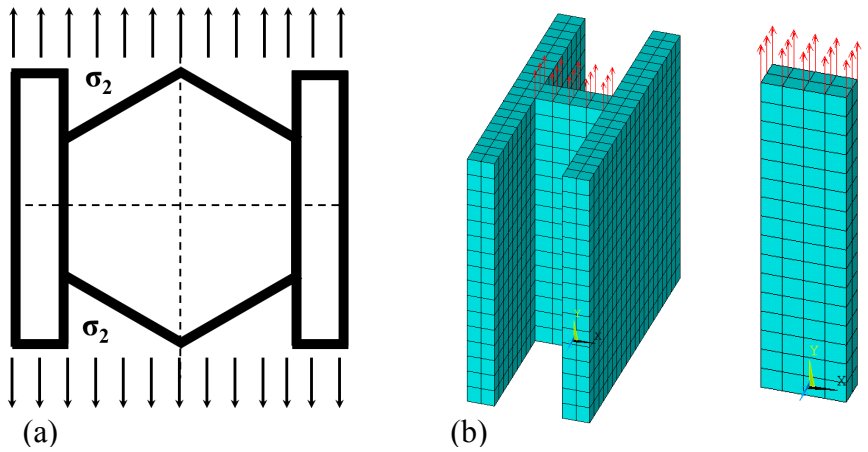

Fig. 3. Unit cell models with the loading scheme to calculate the theoretical elastic modulus along the 2 (vertical) direction (θ≥0): (a) top view; (b) the 'H' and 'I' sections while α=1.0, β =0.1,η=0.125, γ=1, λ=0.1 leading to a coefficient q=0.298.

For a full-size honeycomb structure there are two different cross sections along the 2 direction, the 'H' and the 'I' sections, however only the 'H' section is present when

$\theta<0$. Fig. 3(a) demonstrates the loading scheme of unit cell model to calculate the theoretical elastic modulus along the 2 (vertical) direction for $\theta\geq 0$. It is assumed that the inclined walls of the cell do not contribute significantly to the deformation along the 2 direction, and in the theoretical calculations only the elongations of the 'H' section and the 'I' section are therefore considered. To calculate the elastic modulus E_2 finite element simulations using SOLID 45 element with 8 nodes and three translational degrees have been carried out to obtain the coefficient q which is the ratio between the deformations of the cell structures with the 'H' section and 'I' section being subjected to the same boundary conditions. A total of 1536 elements for the 'H' section and 192 elements for the 'I' section are used in the simulations. Nodal forces are loaded on the top surface as shown in Fig. 3(b) while all three translational degrees of the bottom surface is totally constrained. The deformations of the 'H' and 'I' sections are calculated using the average value of the nodal displacements on the loading surfaces. Fig. 4 shows a map of the coefficient q versus the parameters η and λ for α=1, β=0.1, γ=1. Within the interval of parameters used in these simulations, the value of q ranges between 0.2 and 0.8, with the highest values corresponding to the upper limits of η and λ.

The total deformation along the 2 direction corresponds to the sum of the elongations of the the 'H' section and the 'I' section for $\theta\geq 0$, i.e.:

$$F=\sigma_2 b(2\eta l + 2l\cos\theta) \tag{12}$$

$$\delta_2 = \frac{F\sin\theta}{\eta\lambda b E_s} + q\frac{F\alpha}{2\eta\lambda b E_s} \tag{13}$$

The strain along the 2 direction induced by applying a stress σ_2 can be obtained as:

$$\varepsilon_2 = \frac{\delta_2}{\alpha l + 2l\sin\theta} \tag{14}$$

The homogenized nondimensional Young's modulus along the 2 direction with a $\theta\geq 0$ cell angle can therefore be obtained from the ratio between the tensile stress and strain:

$$\frac{E_2}{E_s} = \frac{\sigma_2}{\varepsilon_2} = \frac{\eta\lambda(\alpha + 2\sin\theta)}{(2\sin\theta + q\alpha)(\eta + \cos\theta)} \tag{15}$$

For the case of the honeycomb with a cell angle of $\theta<0$, only the 'H' section exists. Therefore, following the same mathematical manipulation and when considering the width of the unit cell being αl (and again equal to is $\alpha l+2l\sin(\theta)$ when $\theta\geq 0$), equations (13) and (14) can be rewritten as:

$$\delta_2 = q\frac{F\alpha}{2\eta\lambda bE_s}$$
$$\varepsilon_2 = \frac{\delta_2}{\alpha l} \tag{16}$$

Therefore, the homogenized and nondimensional elastic modulus along the 2 direction with a θ<0 cell angle is:

$$\frac{E_2}{E_s} = \frac{\eta\lambda}{q(\eta + \cos\theta)} \tag{17}$$

As a summary, the elastic modulus of the ZPR honeycomb along the 2 direction can be expressed as:

$$\frac{E_2}{E_s} = \begin{cases} \dfrac{\eta\lambda(\alpha + 2\sin\theta)}{(2\sin\theta + q\alpha)(\eta + \cos\theta)} & for\ \theta \geq 0 \\ \dfrac{\eta\lambda}{q(\eta + \cos\theta)} & for\ \theta < 0 \end{cases} \tag{18}$$

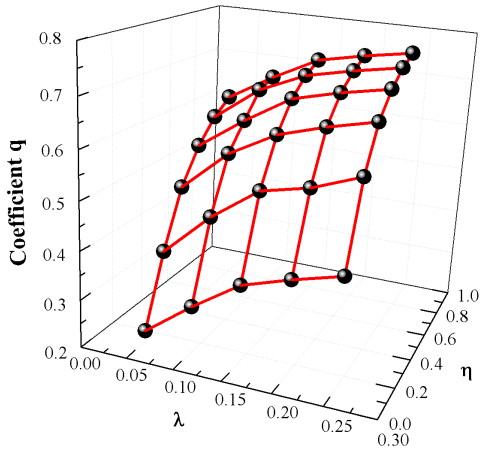

Fig. 4. The coefficient q versus the parameters η and λ for α=1.0, β=0.1, γ=1.0.

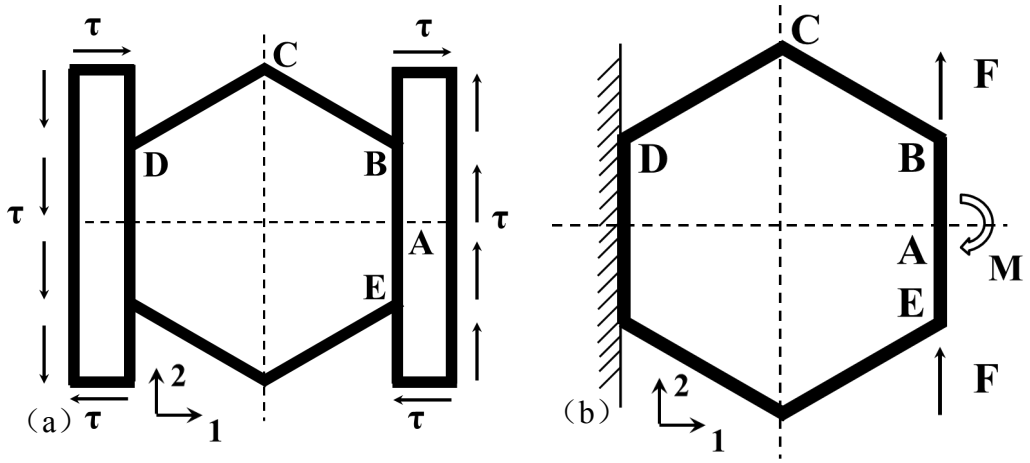

Fig.5. Top view of the unit cell for the in-plane shear model loading (θ≥0)

The loading scheme related to the calculation of the in-plane shear modulus is shown in Fig.5. The unit cell is subjected to an in-plane shear stress, and only the bending deformation of the honeycomb struts is considered. The shear deflection of the thin plate part corresponds to the deformations of points B and E. Because of symmetry, no relative motion between points B and E is also present. The model shown in Fig.5(a) could be therefore simplified into a statically symmetrical indeterminate beam model loaded antisymmetrically (Fig.5(b)). Considering the concentration of the shear stress on point A, one obtains M=0 and:

$$F = \tau b(\frac{1}{2}\alpha l + l\sin\theta) \tag{19}$$

The model has one degree of indeterminacy, which can be solved by using Castigliano's theorem and obtain the displacement of the point B induced by the shear force:

$$\delta_{12} = \frac{\omega F l^3}{3E_s I} \tag{20}$$

Where:

$$\omega = \frac{8\cos^2\theta(\alpha^3 + 3\alpha^2 + 6\alpha\sin\theta + 7\sin^2\theta)}{\alpha^3 + 12\alpha^2 + 24\alpha\sin\theta + 16\sin^2\theta} \tag{21}$$

The shear strain could be calculated by:

$$\gamma_{12} = \frac{\delta_{12}}{2(\eta l + l\cos\theta)} \tag{22}$$

Using G=τ/γ and substituting into equation (19), one can obtain the homogenized

and nondimensional shear modulus as:

$$\frac{G_{12}}{E_s} = \frac{\beta^3(\eta + \cos\theta)}{\omega(\alpha + 2\sin\theta)} \tag{23}$$

For the case of the cell angle θ<0, by following the same solution process and also considering the width of the unit cell as indicated for the previous two cases, one could also obtain the analogous homogenized nondimensional shear modulus:

$$\frac{G_{12}}{E_s} = \frac{\beta^3(\eta + \cos\theta)}{\omega\alpha} \tag{24}$$

Again as a summary, the homogenized nondimensional shear modulus is described as:

$$\frac{G_{12}}{E_s} = \begin{cases} \dfrac{\beta^3(\eta + \cos\theta)}{\omega(\alpha + 2\sin\theta)} \; for \; \theta \geq 0 \\ \dfrac{\beta^3(\eta + \cos\theta)}{\omega\alpha} \; for \; \theta < 0 \end{cases} \tag{25}$$

2.3. Finite element homogenization

The numerical homogenization was performed using the commercial finite element software ANSYS (version 15.0, ANSYS Inc.). The models were developed using 3D structral elements Solid 45 defined by 8 nodes and three translational degrees at each node. The full-size representative volumes used to simulate the in-plane tension along the 1 and 2 directions were given by 5×5 unit cells (Fig. 6 (a)) with boundary conditions following [12, 41]. Convergence tests were performed for the homogenized E_1 and E_2 stress-strain coefficients, resulting in the choice of elements with a minimum uniform size of $t/2$ after the ratio $(|E_i^k - E_i^{k+1}|)/E_i^k$ (with i=1,2 and k correspoding to the k-step of the convergence test) reached a value of 0.5% after 2 steps. The uniform element size was parametrized as t/k. For the in-plane tension along the 1 direction the surfaces A and B were loaded with displacement conditions $u_1=\varepsilon_0 * x_1$, $u_2= u_3=0$ where x_1 was the coordinate of the element nodes and ε_0 the tensile axial strain on the 1 direction, the surfaces C, D, E and F were set as free boundary conditions. In the case of the in-plane tension along the 2 direction the surfaces C and D were loaded with displacements equal to $u_2=\varepsilon_0 * x_2$, $u_1= u_3=0$, where x_2 was the coordinate of the element nodes and ε_0 the tensile axial strain along the 2-direction. The surfaces A, B, E and F were also set as being with free boundary conditions. For the in-plane shear simulation, the representative volumes were given by an one half unit cell shown in Fig. 6(b). The representative volumes were chosen with the purpose of reducing the influence of the thin plate parts' buckling on the shear modulus. Convergence tests were also performed following the 0.5% convergence criteria used for the uniaxial moduli, this time using for the convergence the ratio $(|G_{12}^k - G_{12}^{k+1}|)/G_{12}^k$ and uniform element size parametrized as b_1/k. The final

minimum size of the elements was equal to $b_1/4$. The boundary conditions were applied following [42] by using a cantilever beam clamp. Surface A was set as a fixed end, and surface B was loaded with a displacement condition $u_2=\gamma_0 * L_1$ where γ_0 was the shear strain, and L_1 the total length of the representative volumes along the 1 direction. Surfaces C and D were subjected to anti-symmetrical boundary conditions mimicking a continuous honeycomb along the 2-direction. Surface E was subjected to symmetric boundary conditions due to the structural symmetry. In order to avoid Saint-Venant effects from the borders, the average tensile stress and strain were calculated within the central unit cell (red rectangle in Fig. 6(a)) [42]. The in-plane tensile and shear strains were evaluated using the average displacements of the element nodes in the corresponding volumes. The average tensile and shear stresses were calculated using the following formulation [43]:

$$\bar{\sigma}_{11} = \frac{1}{V}\int_V \sigma_{ii}(1,2,3)dV, \bar{\tau}_{12} = \frac{1}{V}\int_V \tau_{12}dV \tag{26}$$

The stress and strain relations of for a general orthogonal anisotropic material are expressed as:

$$\begin{Bmatrix} \bar{\varepsilon}_1 \\ \bar{\varepsilon}_2 \\ \bar{\varepsilon}_3 \\ \bar{\gamma}_{23} \\ \bar{\gamma}_{13} \\ \bar{\gamma}_{12} \end{Bmatrix} = \begin{bmatrix} S_{11} & S_{12} & S_{13} & 0 & 0 & 0 \\ S_{21} & S_{22} & S_{23} & 0 & 0 & 0 \\ S_{31} & S_{32} & S_{33} & 0 & 0 & 0 \\ 0 & 0 & 0 & S_{44} & 0 & 0 \\ 0 & 0 & 0 & 0 & S_{55} & 0 \\ 0 & 0 & 0 & 0 & 0 & S_{66} \end{bmatrix} \begin{Bmatrix} \bar{\sigma}_1 \\ \bar{\sigma}_2 \\ \bar{\sigma}_3 \\ \bar{\tau}_{23} \\ \bar{\tau}_{13} \\ \bar{\tau}_{12} \end{Bmatrix} \tag{27}$$

Thus the in-plane flexibility of the novel honeycomb could be calculated by:

$$E_1 = 1/S_{11}, E_2 = 1/S_{22}, G_{12} = 1/S_{66} \tag{28}$$

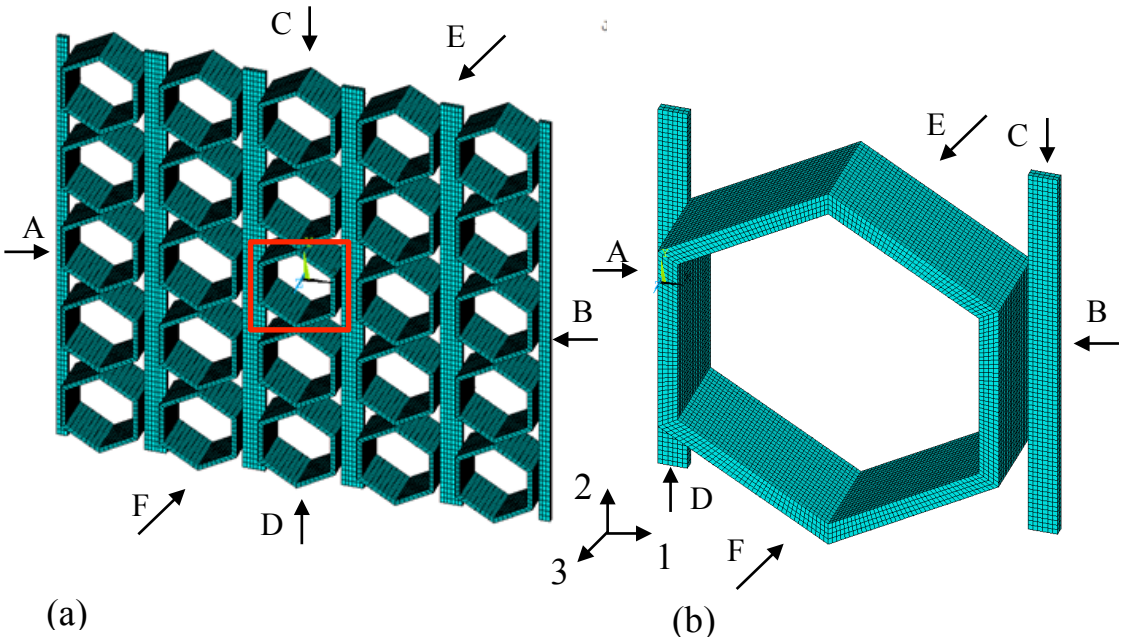

Fig. 6. FE representative volumes: (a) in-plane tension; (b) in-plane shear.

2.4. Manufacturing and experimental tests

All samples used in this work have been manufactured using ABS plastic with a rapid prototyping Fusion Deposition Molding (FDM) Stratasys machine (Stratasys Inc., USA). The elastic mechanical preperties of the core material have been determined following a standard tensile tests (ASTM D638-08) using an Instron 1341 test machine (25KN load cell, 1mm/min) with dog-bone specimens (Type I, T= 5 mm). The dog-bone specimens were also produced with the same FDM rapid prototyping technique. During the tensile tests a video extensometer (Imetrum video gauge system) was used to track the strains both along the load direction and the transverse direction. This video gauge system consists of a high resolution and frame-rate video camera, a telecentric lens and a PC with Imetrum software installed to track and measure the position of the targets placed on the sample. The ABS plastic showed orthotropic elastic mechanical properties, with E_x=2069.5MPa, υ_{xy}=0.38, E_y=2189.5MPa, υ_{yx}=0.46, all consistent with similar work done by other authors [44-46]. The equivalent isotropic properties were estimated using the geometric average value of the orthotropic Young's modulus and the Poisson's ratio values [44], with resulting values of E_s=2129MPa, υ_s=0.42, G_s=749MPa. For convenience, the equivalent isotropic constants were used in the analytical analysis and during the FEM homogenization process.

The in-plane tensile tests to measure the homogenized elastic modulus E_1 and the shear modulus G_{12} were performed using an Instron 3343 testing machine with a 1KN load cell. The in-plane tensile tests to obtain the homogenized Young's modulus E_2 were carried out using an Instron 8872 test machine with a 5KN load cell. Bluehill and Instron Matrix software were used to record the force and displacement values during those tests with a constant displacement rate 1mm/min. The same video

extensometer used in the tests of the dog-bone specimens was also employed to determine the strains both along the loading and transverse directions. The honeycomb samples used in the tensile test along the 1 and 2-directions had dimensions of 174mm×100mm×4mm, and 120mm×89mm×4mm respectively. Because the samples according to standards had wider dimensions than the ones of the grips, all specimens used during the tensile tests were designed to have ends with an appropriate width to fit the grips (Fig. 7). To improve the accuracy of the data acquisition from the video gauge system, speckle patterns were placed on the samples with a black marker pen as tracking targets. Following the ASTM D3518/D3518M-13 standard an off-axial test along 45 deg was performed to determine the homogenized in-plane shear modulus. The samples had in that case dimensions of 187mm×68mm ×5mm. The in-plane shear modulus of the honeycomb could then be calculated from the following expression [47]:

$$G_{12} = \frac{P_x}{2bt(\varepsilon_x - \varepsilon_y)} \tag{29}$$

In (29) b and t are the width and the thickness of the honeycomb respectively. P_x represents the loading force, while ε_x and ε_y are the strains along the loading and transverse directions.

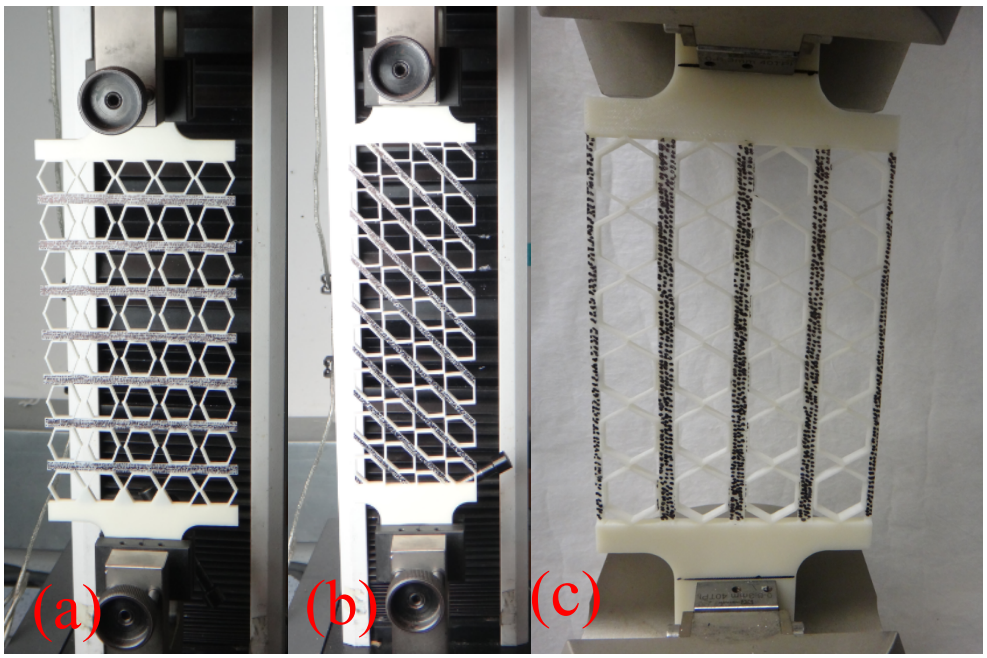

Fig. 7. Honeycomb structures experimental setup: (a) in-plane tensile tests along the 1 direction; (b) off-axial tensile tests along 45 deg direction; (c) in-plane tensile tests along the 2 direction.

3. Results and discussions

The geometrical unit cell parameters of the honeycomb samples used in the experimental tensile tests along the 1 and 2 directions were l=10mm, α=1, β=0.1, $\gamma=b/l$=0.4, η=0.25, λ=0.25, θ=30°. For the off-axis in-plane tensile tests the analogous

paramaters were l=10mm, α=1, β=0.1, $\gamma=b/l$=0.5, η=0.15, λ=0.2, θ=45°. Table 1 shows the comparison between the analytical model, FEM homogenization and the experimental results. For the homogenized tensile modulus E_1, the experimental results show discrepancies of 3.9% with the analytical results, and 4.4% lower than the values predicted by the FE simulations, the latter being 8.7% stiffer than the analytical results. The experimental E_2 modulus show a lower stiffness (10.34% and 8.83%) than the analytical and FE results respectively, however the analytical results show a difference of 1.68% only over the FE homogenization results for that specific configuration. The experimental values for the in-plane shear modulus show however discrepancies between 19.7% and 5.8% over the analytical and the FE results respectively. The in-plane shear modulus also shows a difference of 11.6% between the analytical and the FE simulations. Uncertainties affecting the results among the three sets of data can be ascribed to a variety of reasons. The samples manufactured using the FDM technics have a layerwise deposition and an additional degree of interal porosity that do not meet the assumption of a homogeneous and isotropic honeycomb material [16, 44, 46]. The assumption to neglect the contribution from the inclined walls taken to calculate the analytical expression of E_2 leads to slightly lower values than the FE ones. For the in-plane shear modulus, not taking the deformation of the thin plate part into account in the analytical model which is considered in the FE homogenization also produces some difference between results. Moreover, the analytical model to describe the in-plane shear modulus is generated from a pure shear model, and there are generally three major loading types to simulate a pure in-plane shear deformation (uniaxial, biaxial and tangential loading [48]). In this work, the uniaxial loading is used in the experimental tests, while the tangential loading is applied to the FE homogenization. Even when the fixtures produce a pure shear deformation as closely as possible to the ideal case, there are still differences between a pure shear deformation and an approximate one [42].

Fig. 8 shows the variation of the Poisson's ratio ν_{12} against strain on the loading direction during the tensile test along the 1 direction. After an initail slack in taking up the load, the samples exhibit a stable in-plane Poisson's ratio of -0.02. The small non-zero value of the Poisson's ratio can be explained by noting that the transverse strain was measured from the thin plate parts, which were undergoing a non homogeneous tensile stress distribution that led some parts of the thin plate connected to the hexagonal structures shortened, while other parts between the hexagonal units were extended. The combined actions led to a small non-zero deformation on the transverse direction, similarly to what observed in the experimental testing of zero-ν SILICOMB structure [17].

Table 1. Comparison of the analytical, FEM, and experimental results

	Analytical	FEM	Experimental
E_1 (MPa)	7.68	8.35	7.98±0.15
E_2 (MPa)	154.78	152.22	138.78±5.31
G_{12} (MPa)	0.61	0.69	0.73±0.01

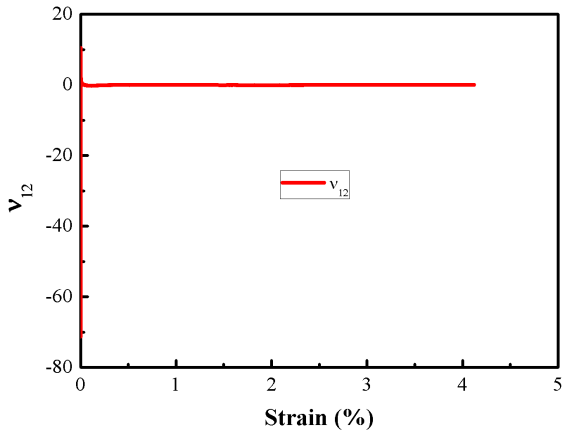

Fig. 8. The Poisson's ratio ν_{12} against strain curve

4. Parametric analysis

From equations (11), (18) and (25) one can perform a parametric analysis to identify the sensivitivity of the in-plane stiffness of the honeycomb versus the geometric parameters. For this analysis l is set constant (10mm) for all the calculations. Figs. 9-11 show the variation of the homogenized non-dimensional elastic modulus of the novel honeycomb along the 1 direction versus the different geometrical parameters of the unit cell. The results are generated through the FE homogenization and compared to the analogous analytical simulations. The novel honeycomb has a core hexagonal structure that produces a very similar in-plane stiffness as the one described by the Gibson and Ashby model for classical centersymmetric hexagonal configurations [1, 49]. In the proximity of 0° the shear deformation contributes substantially to the whole honeycomb deformation, leading to a larger discrepancy between the analytical results and the FE homogenization because the analytical model does not take into account the shear deformation of the bending ligaments. However, when the absolute value of the cell angle is relatively large ($\theta \geqslant 10°$ or $\theta < -10°$), the analytical results show in general a very good agreement with the FE homogenization. For example, when θ=45°, α=1, β=0.1, η=0.25, γ=1, λ=0.1 the analytical result is only 0.64% stiffer compared to the analogous one from the FE simulation. Fig. 9 shows the finite element and analytical predictions of the non-dimensional in-plane elastic modulus E_1/E_s versus the cell angle for various parameters α and β=0.1, η=0.25, γ=1, λ=0.1. An increasing cell wall aspect ratio α leads to a decrease of the in-plane tensile modulus. For an internal cell angle of 5°, one can observe a steep decrease (44%) on the in-plane tensile modulus when α varies from 1.0 to 2.0. Fig. 10 shows the values of the nondimensional modulus E_1/E_s versus the cell angles at different β values and constant α=1.0, η=0.25, γ=1, λ=0.1. The increase of the cell wall aspect ratio β leads to a sharp increase of the in-plane tensile modulus, for instance the in-plane tensile modulus shows a very great increase (629%, θ=45°) when the parameter β varies from 0.05 to 0.10. It provides a good way to design the in-plane tensile modulus by various parameter β. Fig. 11 describes the FE homogenization and analytical predictions of

the non-dimensional in-plane elastic modulus E_1/E_s versus the cell angles for various parameters η while α=1.0, β=0.1, γ=1, λ=0.1. The increase of the parameter could bring to a less significant increase in the in-plane tensile modulus.

The connecting plate part appears to be one of the main factors affecting the in-plane elastic modulus E_2. Figs. 12 and 13 show the behaviour of the nondimensional in-plane modulus E_2/E_s versus the geometric parameters describing the thin plate part contribution. In general the increase of the parameters η and λ leads to an increase of the cross sectional area when other parameters remain constants and therefore result in a stiffer honeycomb along the 2-direction. The nondimensional modulus increases by 49.1% when the geometric parameter η varies from 0.25 to 0.50, however this increase is lower (23.5%) in the case of η varying from 0.50 to 0.75 (Fig. 12). The behaviour indicates that the sensitivity of the normalised modulus E_2/E_s is lower towards higher values of the length of the connecting horizontal plate. Fig. 13 shows however that the sensitivity of modulus versus the parameter λ is more uniform, with E_2/E_s globally increasing by 265.1% when λ varies from 0.05 to 0.20.

Figs. 14-16 illustrate the dependence of the in-plane shear modulus G_{12}/E_s versus the different geometric parameters of the unit cell. The analytical equations show a general close comparison with the trends followed by the results of the FE homogenization, although the differences provided by the different boundary conditions seem to be quite consistent, especially for positive internal cell angles. In general an increase of the internal cell angle of the unit cell results in a decrease of the in-plane shear modulus. Similarly, an increase of the cell wall aspect ratio α leads to a decrease of the in-plane shear modulus. Fig. 15 also shows that the both the FE homogenization and the analytical predictions agree on the strong sensitivity versus the cell wall thickness aspect ratio β, with the non-dimensional in-plane shear modulus passing from 4.5×10^{-5} to 1.02×10^{-3} when the parameter β varies from 0.05 to 0.15 for the structure at 45 deg internal cell angle. However, the increase of the variable η with the other parameters kept constant leads to an increase of the in-plane shear modulus, although much less significant than the one provided by varying the parameter β (Fig. 16). The results also indicate that the increase of η further results in an increase of the discrepancies between the analytical results and the FE results, because in the analytical model the deformation of the thin plate is neglected.

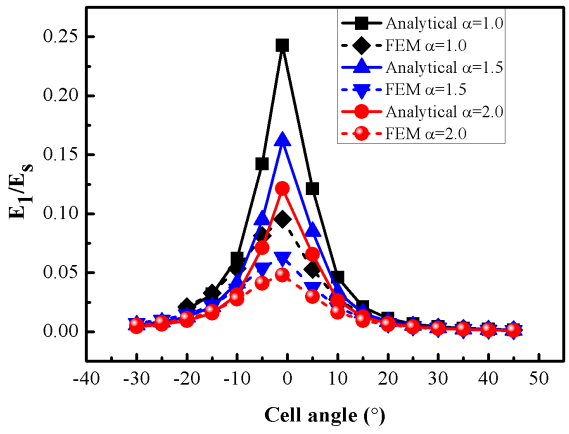

Fig. 9. FE homogenization and analytical predictions of the non-dimensional in-plane elastic modulus E_1/E_s versus the cell angles for various parameters α while β=0.1, η=0.25, γ=1, λ=0.1.

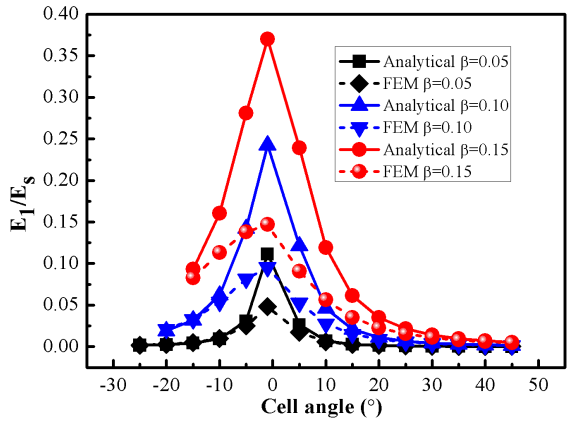

Fig. 10. FE homogenization and analytical predictions of the non-dimensional in-plane elastic modulus E_1/E_s versus the cell angles for various parameters β at α=1.0, η=0.25, γ=1, λ=0.1.

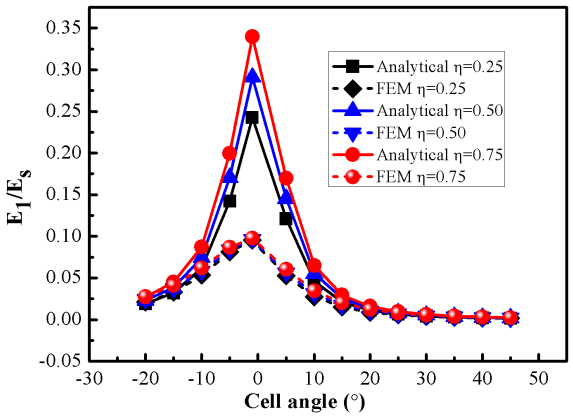

Fig. 11. FE homogenization and analytical predictions of the non-dimensional in-plane elastic modulus E_1/E_s versus the cell angles for various parameters η while α=1.0, β=0.1, γ=1, λ=0.1.

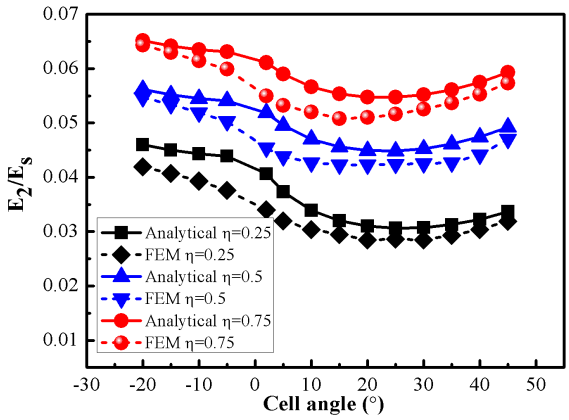

Fig. 12. FE homogenization and analytical predictions of the non-dimensional in-plane tension modulus E_2/E_s versus the cell angles for various parameters η while α=1.0, β=0.1, γ=1, λ=0.1.

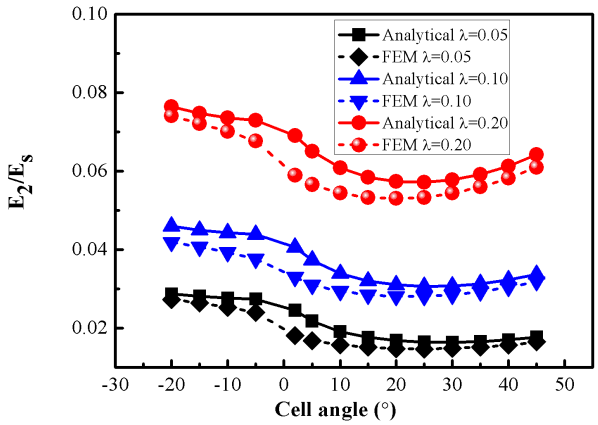

Fig. 13. FE homogenization and analytical predictions of the non-dimensional in-plane tension modulus E_2/E_s versus the cell angles for various parameters λ while α=1.0, β=0.1, γ=1, η=0.25.

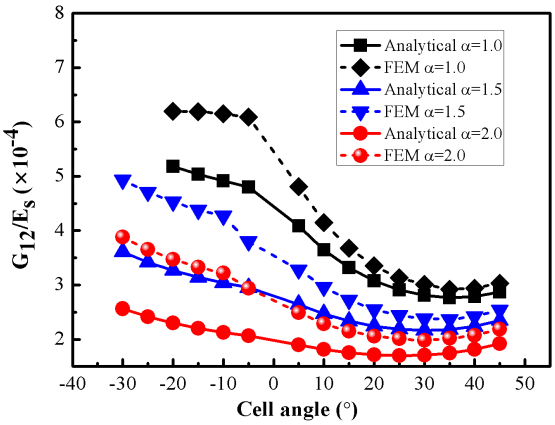

Fig. 14. FE homogenization and analytical predictions of the non-dimensional

in-plane shear modulus G_{12}/E_s versus the cell angles for various parameters α while β=0.1, η=0.15, γ=1, λ=0.1.

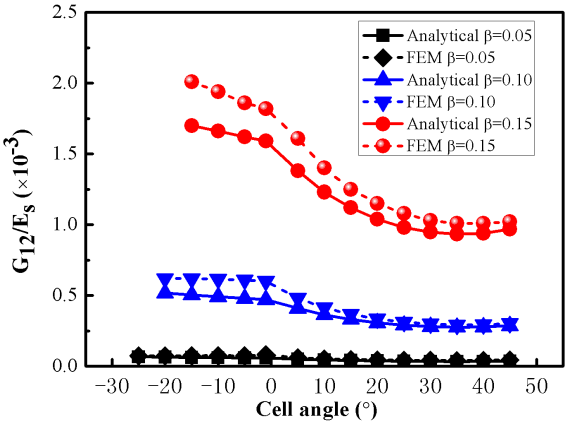

Fig. 15. FE homogenization and analytical predictions of the non-dimensional in-plane shear modulus G_{12}/E_s versus the cell angles for various parameters β while α=1.0, η=0.15, γ=1, λ=0.1.

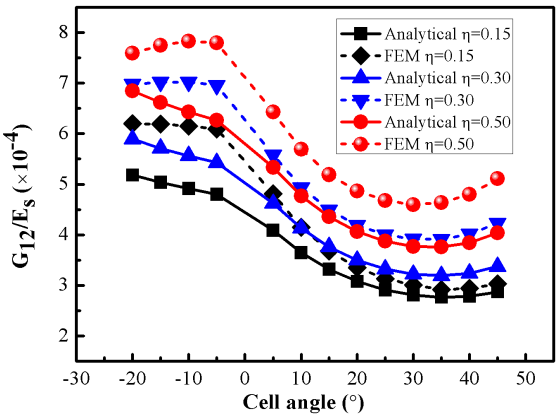

Fig. 16. FE homogenization and analytical predictions of the non-dimensional in-plane shear modulus G_{12}/E_s versus the cell angles for various parameters η while α=1.0, β=0.1, γ=1, λ=0.1.

5. Conclusions

The novelty of the zero Poisson's ratio honeycomb topology proposed in this work consists in assembling two geometrical entities such as hexagonal structures to bear the out-of-plane compression and to produce in-plane flexibility, and a connecting a thin plate for the large out-of-plane flexibility. These entities provide different contributions to the effective mechanical properties and lead to a separate design for the in-plane and out-of-plane performances. The analytical and FE homogenization models for the in-plane tension modulus along both the two directions and the in-plane shear modulus have been validated by a series of experimental tests following ASTM standards. The parametric analyses show that it is possible to obtain

large variations and control of the design of the in-plane mechanical properties through the variation of the unit cell geometric parameters.

Acknowledgements

The supports of the FP7-AAT.2012.6.3-1-341509 project MorphElle (www.morphelle.eu) and the National Natural Science Foundation of China (Grant No.11225211) are gratefully acknowledged. Jian Huang would also thank the British Council and the Chinese Scholarship Council (CSC) for the funding of his research work at the University of Bristol.

References

[1] Gibson LJ, Ashby MF. Cellular solids: structure and properties: Cambridge university press; 1997.

[2] Bitzer T. Honeycomb technology: materials, design, manufacturing, applications and testing: Springer Science & Business Media; 1997.

[3] Scarpa F, Tomlin P. On the transverse shear modulus of negative Poisson's ratio honeycomb structures. Fatigue & Fracture of Engineering Materials & Structures. 2000;23(8):717-20.

[4] Lim TC. Functionally graded beam for attaining Poisson-curving. Journal of materials science letters. 2002;21(24):1899-901.

[5] Bezazi A, Scarpa F, Remillat C. A novel centresymmetric honeycomb composite structure. Composite Structures. 2005;71(3):356-64.

[6] Grima JN, Gatt R, Alderson A, Evans KE. On the potential of connected stars as auxetic systems. Molecular Simulation. 2005;31(13):925-35.

[7] Sun J, Scarpa F, Liu Y, Leng J. Morphing thickness in airfoils using pneumatic flexible tubes and Kirigami honeycomb. Journal of Intelligent Material Systems and Structures. 2015:1045389X15580656.

[8] Prall D, Lakes R. Properties of a chiral honeycomb with a Poisson's ratio of—1. International Journal of Mechanical Sciences. 1997;39(3):305-14.

[9] Miller W, Smith CW, Scarpa F, Evans KE. Flatwise buckling optimization of hexachiral and tetrachiral honeycombs. Composites Science and Technology. 2010;70(7):1049-56.

[10] Lorato A, Innocenti P, Scarpa F, Alderson A, Alderson KL, Zied KM, et al. The transverse elastic properties of chiral honeycombs. Composites Science and Technology. 2010;70(7):1057-63.

[11] Alderson A, Alderson KL, Attard D, Evans KE, Gatt R, Grima JN, et al. Elastic constants of 3-, 4- and 6-connected chiral and anti-chiral honeycombs subject to uniaxial in-plane loading. Composites Science and Technology. 2010;70(7):1042-8.

[12] Chen YJ, Scarpa F, Liu YJ, Leng JS. Elasticity of anti-tetrachiral anisotropic lattices. International Journal of Solids and Structures. 2013;50(6):996-1004.

[13] Evans KE, Nkansah MA, Hutchinson IJ, Rogers SC. Molecular Network Design. Nature. 1991;353(6340):124.

[14] Lim T-C. Auxetic Materials and Structures: Springer; 2015.

[15] Lira C, Scarpa F, Olszewska M, Celuch M. The SILICOMB cellular structure: Mechanical and dielectric properties. physica status solidi (b). 2009;246(9):2055-62.

[16] Lira C, Scarpa F, Tai YH, Yates JR. Transverse shear modulus of SILICOMB cellular structures. Composites Science and Technology. 2011;71(9):1236-41.

[17] Virk K, Monti A, Trehard T, Marsh M, Hazra K, Boba K, et al. SILICOMB PEEK Kirigami

cellular structures: mechanical response and energy dissipation through zero and negative stiffness. Smart Materials and Structures. 2013;22(8):084014.
[18] Neville RM, Monti A, Hazra K, Scarpa F, Remillat C, Farrow IR. Transverse stiffness and strength of Kirigami zero-ν PEEK honeycombs. Composite Structures. 2014;114:30-40.
[19] Grima JN, Oliveri L, Attard D, Ellul B, Gatt R, Cicala G, et al. Hexagonal honeycombs with zero Poisson's ratios and enhanced stiffness. Advanced Engineering Materials. 2010;12(9):855-62.
[20] Grima JN, Attard D. Molecular networks with a near zero Poisson's ratio. physica status solidi (b). 2011;248(1):111-6.
[21] Attard D, Grima JN. Modelling of hexagonal honeycombs exhibiting zero Poisson's ratio. physica status solidi (b). 2011;248(1):52-9.
[22] Olympio KR, Gandhi F. Zero Poisson's Ratio Cellular Honeycombs for Flex Skins Undergoing One-Dimensional Morphing. Journal of Intelligent Material Systems and Structures. 2009;21(17):1737-53.
[23] Olympio K, Gandhi F. Zero-v Cellular Honeycomb Flexible Skins for One-Dimensional Wing Morphing. 48th AIAA/ASME/ASCE/AHS/ASC Structures, Structural Dynamics, and materials Conference, 23-26 April 2007, Honolulu, Hawaii.
[24] Alderson A, Alderson KL, Chirima G, Ravirala N, Zied KM. The in-plane linear elastic constants and out-of-plane bending of 3-coordinated ligament and cylinder-ligament honeycombs. Composites Science and Technology. 2010;70(7):1034-41.
[25] Evans K. The design of doubly curved sandwich panels with honeycomb cores. Composite Structures. 1991;17(2):95-111.
[26] Lakes R. Foam structures with a negative Poisson's ratio. Science. 1987;235(4792):1038-40.
[27] Masters I, Evans K. Models for the elastic deformation of honeycombs. Composite structures. 1996;35(4):403-22.
[28] Evans K, Alderson K. Auxetic materials: the positive side of being negative. Engineering Science and Education Journal. 2000;9(4):148-54.
[29] Grima JN, Manicaro E, Attard D. Auxetic behaviour from connected different-sized squares and rectangles. Proceedings of the Royal Society A: Mathematical, Physical and Engineering Sciences. 2010;467(2126):439-58.
[30] Kimizuka H, Kaburaki H, Kogure Y. Mechanism for negative Poisson ratios over the α-β transition of cristobalite, SiO 2: a molecular-dynamics study. Physical Review Letters. 2000;84(24):5548.
[31] Engelmayr GC, Cheng M, Bettinger CJ, Borenstein JT, Langer R, Freed LE. Accordion-like honeycombs for tissue engineering of cardiac anisotropy. Nature materials. 2008;7(12):1003-10.
[32] Bubert EA, Woods BKS, Lee K, Kothera CS, Wereley NM. Design and Fabrication of a Passive 1D Morphing Aircraft Skin. Journal of Intelligent Material Systems and Structures. 2010;21(17):1699-717.
[33] Olympio KR, Gandhi F. Flexible Skins for Morphing Aircraft Using Cellular Honeycomb Cores. Journal of Intelligent Material Systems and Structures. 2009;21(17):1719-35.
[34] Gong X, Huang J, Scarpa F, Liu Y, Leng J. Zero Poisson's ratio cellular structure for two-dimensional morphing applications. Composite Structures. 2015;134:384-92.
[35] Barbarino S, Bilgen O, Ajaj RM, Friswell MI, Inman DJ. A review of morphing aircraft. Journal of Intelligent Material Systems and Structures. 2011;22(9):823-77.
[36] Min Z, Kien VK, Richard LJY. Aircraft morphing wing concepts with radical geometry change.

The IES Journal Part A: Civil & Structural Engineering. 2010;3(3):188-95.
[37] Rodriguez AR. Morphing aircraft technology survey. 45th AIAA aerospace sciences meeting and exhibit2007. p. 2007-1258.
[38] Gomez JC, Garcia E. Morphing unmanned aerial vehicles. Smart Materials and Structures. 2011;20(10):103001.
[39] Sobieszczyk P, Majka M, Kuźma D, Lim TC, Zieliński P. Effect of longitudinal stress on wave propagation in width‐constrained elastic plates with arbitrary Poisson's ratio. physica status solidi (b). 2015;252(7):1615-9.
[40] Young WC, Budynas RG. Roark's formulas for stress and strain: McGraw-Hill New York; 2002.
[41] Odegard GM. Constitutive modeling of piezoelectric polymer composites. Acta materialia. 2004;52(18):5315-30.
[42] Singer J, Arbocz J, Weller T. Buckling Experiments: Experimental Methods in Buckling of Thin-walled Structures. Shells, Built-up Structures, Composites and Additional Topics: John Wiley & Sons; 2002.
[43] Sun C, Vaidya R. Prediction of composite properties from a representative volume element. Composites Science and Technology. 1996;56(2):171-9.
[44] Lira C, Scarpa F. Transverse shear stiffness of thickness gradient honeycombs. Composites Science and Technology. 2010;70(6):930-6.
[45] Ahn S-H, Montero M, Odell D, Roundy S, Wright PK. Anisotropic material properties of fused deposition modeling ABS. Rapid Prototyping Journal. 2002;8(4):248-57.
[46] Bellini A, Güçeri S. Mechanical characterization of parts fabricated using fused deposition modeling. Rapid Prototyping Journal. 2003;9(4):252-64.
[47] Shen G, Hu G. Mechanics of Composite Materials: Tsinghua University Press; 2006.
[48] Salit V, Weller T. On the feasibility of introducing auxetic behavior into thin-walled structures. Acta Materialia. 2009;57(1):125-35.
[49] Scarpa F, Panayiotou P, Tomlinson G. Numerical and experimental uniaxial loading on in-plane auxetic honeycombs. The Journal of Strain Analysis for Engineering Design. 2000;35(5):383-8.